The Astrophysical Journal, 887:111 (17pp), 2019 December 20 https://doi.org/10.3847/1538-4357/ab53df

Mapping Spatial Variations of H I Turbulent Properties in the Small and Large Magellanic Cloud

Samuel Szotkowski[1], Delano Yoder[1], Snežana Stanimirović[1], Brian Babler[1], N. M. McClure-Griffiths[2], Helga Dénes[3], Alberto Bolatto[4], Katherine Jameson[2], and Lister Staveley-Smith[5]

[1] Astronomy Department, University of Wisconsin—Madison, 475 North Charter Street, Madison, WI 53706-1582, USA
[2] Research School of Astronomy & Astrophysics, Australian National University, Weston Creek, ACT, Australia
[3] ASTRON, The Netherlands Institute for Radio Astronomy, Dwingeloo, The Netherlands
[4] Department of Astronomy, University of Maryland, College Park, MD 20742, USA
[5] ICRAR, University of Western Australia, Crawley, Perth, WA, Australia
Received 2019 August 5; revised 2019 October 16; accepted 2019 November 2; published 2019 December 16

Abstract

We developed methods for mapping spatial variations of the spatial power spectrum (SPS) and structure function slopes, with the goal of connecting the statistical properties of neutral hydrogen (H I) with the turbulent drivers. The new methods were applied to the H I observations of the Small and Large Magellanic Clouds (SMC and LMC). In the case of the SMC, we find highly uniform turbulent properties of H I, with no evidence for local enhancements of turbulence due to stellar feedback. These properties could be caused by a significant turbulent driving on large scales. Alternatively, the significant line-of-sight depth of the SMC could be masking out localized regions with a steeper SPS slope caused by stellar feedback. In contrast to the SMC, the LMC H I shows a large diversity in terms of its turbulent properties. Across most of the LMC, the small-scale SPS slope is steeper than the large-scale slope due to the presence of the H I disk. On small spatial scales, we find several areas of localized steepening of the SPS slope around major H II regions, with the 30 Doradus region being the most prominent. This is in agreement with predictions from numerical simulations, which suggest a steepening of the SPS slope due to stellar feedback that erodes and destroys interstellar clouds. We also find a localized steepening of the large-scale SPS slope in the outskirts of the LMC. This is likely caused by the flaring of the H I disk, or alternatively, by ram-pressure stripping of the LMC disk due to the interactions with the surrounding halo gas.

Unified Astronomy Thesaurus concepts: Interstellar atomic gas (833); Magellanic Clouds (990); Interstellar medium (847); Neutral hydrogen clouds (1099)

1. Introduction

Turbulence is an important structuring agent in the interstellar medium (ISM), and it is thought to be responsible in part for the formation of molecular clouds as well as of the complex structure found in spectral-line images (Elmegreen & Scalo 2004). Many observational studies have revealed a fractal (self-similar, scale-free) nature in distributions of interstellar gas and dust, which, when compared with theory and terrestrial turbulence experiments, indicate that turbulence is an important process in the ISM. This turbulence is often characterized by estimating the spatial power spectrum (SPS) of intensity fluctuations, relating them to the power spectra of the underlying velocity or density fluctuations, and illuminating the spatial scales at which energy is injected or dissipated, as well as the mechanisms by which this energy cascades from large to small scales or vice versa. Many physical processes, including gravitational instabilities (Wada et al. 2002; Bournaud et al. 2010; Krumholz & Burkhart 2016) and stellar feedback (Kim et al. 2001; de Avillez & Breitschwerdt 2005; Joung & Mac Low 2006), have been considered as possible drivers of interstellar turbulence, however, their relative importance remains an open question.

Stellar feedback, in particular, has been considered as a key agent for establishing the hierarchy of structures in the ISM. For example, Grisdale et al. (2017) ran numerical simulations and showed that feedback both removes gas and destroys interstellar and giant molecular clouds (GMCs), effectively shifting the power from small to large scales. In particular, they simulated galaxies like the Small and Large Magellanic Clouds (SMC and LMC), with and without including stellar feedback, and showed the change of the SPS slope on both small and large scales when feedback was included. In a follow-up study, Grisdale et al. (2018) investigated the places where feedback has the first impact—GMCs—and concluded that it is necessary to include effective feedback in numerical simulations to reproduce the observed properties of GMCs.

In this study we continue our investigation of spatial variations of turbulent properties as a way of quantifying the importance of stellar feedback, gravity, and ram pressure as structuring agents of the neutral hydrogen (H I) distribution in galaxies. We focus here on the SMC and LMC as they are especially handy targets because they are close by (50 kpc for the LMC and 60 kpc for the SMC; Westerlund 1991), with a wealth of high-resolution observations. They also allow us to probe large spatial dynamic ranges. The SMC and the LMC are part of a three-galaxy interacting system in which the Milky Way (MW) is the most massive player. Both the LMC and the SMC have a lower mass and metallicity than the MW, $1/2$ solar for the LMC and $1/5$ solar for the SMC (Dufour 1984; Russell & Dopita 1992).

Nestingen-Palm et al. (2017) compared H I turbulent properties between the main star-forming body and outskirts of the SMC. The authors did not find any significant difference either when they mainly probed the density or velocity fluctuations, suggesting that large-scale turbulent driving may be more prominent than stellar feedback in the SMC. In the present study we develop a new technique for mapping out the slope of the H I turbulent spectrum across the SMC and LMC.

Our goal is to connect turbulent properties with the underlying physical processes.

Turbulent properties of H I and dust in the SMC and LMC have been investigated in numerous prior studies. The H I SPS of the SMC has been known not to show any breaks or turnovers (Stanimirović et al. 1999; Stanimirović & Lazarian 2001), suggesting significant energy injection on spatial scales larger than the size of the SMC. The LMC H I SPS, however, has shown a break at 100–200 pc, which was interpreted as being due to disk geometry (Elmegreen et al. 2001; Padoan et al. 2001). Similar findings have been reported for the dust column density, no breaks in the case of the SMC (Stanimirović et al. 2000), and a clear break in the case of the LMC (Block et al. 2010). In the case of the SMC, the dust column density SPS slope agreed with the SPS slope of the H I column density, supporting the idea that gas and large dust grains are well mixed in the ISM. In the case of *Spitzer* observations of the LMC, the SPS slopes were found to be slightly steeper for longer wavelengths, suggesting that cooler dust emission is smoother than the hot dust emission (Block et al. 2010).

Several additional studies have found breaks in the SPS (Elmegreen et al. 2003; Dutta et al. 2009a, 2009b). Combes et al. (2012) found an SPS slope of −1.0 to −1.5 on spatial scales >500 pc in M33 and a slope of −3.0 to −4.0 on smaller spatial scales, with a break at 100–200 pc observed using several tracers. Moreover, the H I SPS slope has been shown to depend on the thickness of velocity channels, with narrow channels largely probing velocity fluctuations, while thick channels largely probe density fluctuations (Lazarian & Pogosyan 2000; Stanimirović & Lazarian 2001). In addition, Lazarian & Pogosyan (2004) showed theoretically that the SPS slope can be affected by optical depth. While in the SMC the fraction of cold H I is small, ∼20% (Jameson et al. 2019), and the optical depth correction is not significant (Nestingen-Palm et al. 2017), the LMC has a CNM fraction of ∼33% (Dickey et al. 2000) and likely a more significant correction for high optical depth. While Braun (2012) estimated a correction factor of 1.3 for the LMC based on H I emission spectra alone, understanding the magnitude of the optical depth correction fully will require future H I absorption observations for many radio sources behind the LMC.

From early studies it was apparent that the SMC and LMC H I SPS slopes are different. Muller et al. (2004) also noted significantly different SPS slopes for four regions in the Magellanic Bridge between the SMC and LMC. These differences of turbulent properties on kiloparsec scales in the Bridge were interpreted as likely tracing different origin (age and physical properties) of gaseous arms pulled out of the SMC. Some small spatial variations of H I turbulent properties across the SMC were noted by Burkhart et al. (2010), where skewness and kurtosis were used to estimate the sonic Mach number based on a relationship found in numerical simulations. H I observations of many other nearby galaxies were used to study turbulent properties via fitting of averaged H I velocity profiles (Young & Lo 1996; Tamburro et al. 2009; Warren et al. 2012; Stilp et al. 2013). It was commonly found that the line width of broad H I components decreases with galactocentric radius. One interpretation of this trend is the decrease of turbulent energy due to lack of stellar feedback. The Burkhart et al. (2010) method was also applied to a set of spiral galaxies from The H I Nearby Galaxy Survey (THINGS) in Maier et al. (2016). Generally, uniform statistical moments were found across galaxies without an obvious correlation between moments and star-forming regions. However, this study had a resolution of about 700 pc and the statistical moments likely trace only large-scale turbulence. While Dutta et al. (2009b) indicated that dwarf galaxies with a higher star formation rate (SFR) per unit area have steeper H I SPS based on a sample of seven galaxies, Zhang et al. (2012) found a lack of correlation between the SPS slope and the SFR surface density for a subsample of LITTLE THINGS dwarf irregular galaxies.

This paper is organized in the following way. In Section 2 we summarize new and existing data sets used in this study. Section 3 explains our rolling SPS and structure function (SF) approach for mapping out spatial variability of turbulent properties across the SMC and LMC. We also summarize here how we produce simple images where we know the SPS slope to test and constrain biases involved with our rolling methods. Several of our tests are documented in the Appendix section. Sections 4 and 5 present our results and compare SPS/SF slopes with the star formation rate and stellar surface densities. Finally, we discuss and conclude our results in Section 6.

2. Data

2.1. SMC and LMC H I Observations

2.1.1. ATCA+Parkes H I Observations of the SMC and LMC

The neutral hydrogen (H I) data cube of the SMC used in this study is from Stanimirović et al. (1999). This is a combination of an aperture-synthesis mosaic obtained with the Australia Telescope Compact Array (ATCA) and single-dish observations obtained with the Parkes 64 m telescope. The two data sets were combined in the image domain; the restoring beam size is 98″. The cube contains 78 velocity channels, each with a velocity resolution of 1.65 km s^{-1}. The H I column density noise level is 4.2×10^{18} cm^{-2} per 1.65 km s^{-1} velocity channel. For further details, see Stanimirović et al. (1999).

The H I data cube for the LMC is from Kim et al. (2003). The Parkes H I observations with the multi-beam receiver (Staveley-Smith et al. 2003) were combined with the ATCA aperture-synthesis mosaic from Kim et al. (1998), resulting in a final data set with an angular resolution of 1′ and a column density sensitivity of 7.2×10^{18} per 1.65 km s^{-1} velocity channels. The image combination of interferometric and single-dish data was performed in the Fourier domain using the Miriad task IMMERG. For further details, see Kim et al. (2003).

2.1.2. ASKAP+Parkes H I Observations of the SMC

This study also includes recently released SMC H I data from the Australian Square Kilometer Array Pathfinder (ASKAP) as part of Commissioning and Early Science observations. ASKAP is an interferometer with 36 12 m dishes, each with a phased array feed. These observations used only 16 ASKAP antennas (McClure-Griffiths et al. 2018). The total integration time was 36 hr in one continuous pointing. ASKAP data were calibrated using the ASKAPSoft pipeline (Cornwell et al. 2011) and were imaged with Miriad. The ASKAP data were combined in the Fourier domain with Parkes data from the HI4PI survey (HI4PI Collaboration et al. 2016). The column density sensitivity of the combined data set is 5.0×10^{18} per 3.9 km s^{-1} velocity channels, which is a factor of two lower than that of the ATCA+Parkes data cube. With the beam size of 27″ × 35″, this data set (Figure 1) is sensitive to linear scales from 10 pc to 5.3 kpc.

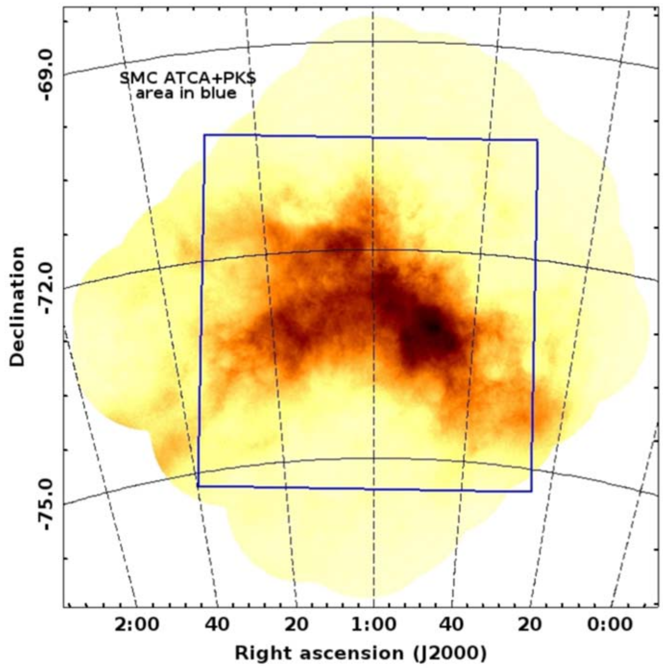

Figure 1. The H I integrated intensity image of the SMC obtained with ASKAP + HI4PI data (McClure-Griffiths et al. 2018). To produce this image, the H I data cube was integrated over the velocity range of (46.5–238.0 km s^{-1}). The angular resolution is $27'' \times 35''$. The footprint of the SMC HI ATCA + Parkes data from Stanimirović et al. (1999) is shown in blue.

2.2. Star Formation Rate

Following Bolatto et al. (2011) and Jameson et al. (2016), we combine Hα and 24 μm images to trace recent star formation. The Hα image of the SMC is from the Magellanic Cloud Emission Line Survey (MCELS; Smith & Team 1999), and has a resolution of $2\rlap{.}''3$. The Hα image of the LMC is from the Southern Hα Sky Survey Atlas (Gaustad et al. 2001), and has a resolution of $0\rlap{.}'8$. For both the SMC and LMC, the 24 μm images are from the *Spitzer* Survey "Surveying the Agents of Galaxy Evolution" (SAGE; Gordon et al. 2011). To estimate the SFR surface density, we follow the prescription by Calzetti et al. (2007),

$$\mathrm{SFR}(M_\odot\ \mathrm{yr}^{-1}) = 5.3 \times 10^{-42}[L(\mathrm{H}\alpha) + (0.031 \pm 0.006)L(24\ \mu\mathrm{m})], \quad (1)$$

where $L(\mathrm{H}\alpha)$ and $L(24\ \mu\mathrm{m})$ are the luminosities of Hα and 24 μm images in units of erg s^{-1}. The SFR image has an rms noise value of $4 \times 10^{-4}\ M_\odot\ \mathrm{yr}^{-1}\ \mathrm{kpc}^{-2}$ and $1 \times 10^{-4}\ M_\odot\ \mathrm{yr}^{-1}\ \mathrm{kpc}^{-2}$ for the SMC and LMC, respectively.

3. Methods

3.1. Spatial Power Spectrum

We apply a method similar to one that was used in previous studies (Crovisier & Dickey 1983; Green 1993; Stanimirović et al. 1999; Elmegreen 2000). For a 2D image $I(x)$, the 2D SPS is defined as

$$P(k) = \int\int \langle I(x) I(x') \rangle\, e^{i\boldsymbol{L}\cdot\boldsymbol{k}}\, d\boldsymbol{L}, \quad (2)$$

where k is the spatial frequency, measured in units of wavelength, and is proportional to the inverse of the spatial scale, while $\boldsymbol{L} = \boldsymbol{x} - \boldsymbol{x}'$ is the distance between two points.

We first regrid the H I images to ensure independent pixels, with each pixel having an angular size equal to that of the telescope beam. Then we take the Fourier transform and square the modulus of the transform, $\langle \mathfrak{R}^2 + \mathfrak{I}^2 \rangle$ (where $\mathfrak{R}$ and $\mathfrak{I}$ are the real and imaginary parts of the 2D Fourier transform), which we refer to as the modulus image. A range of annuli is then selected in the modulus image, spaced evenly apart by $0.05\log(k)$. Within each annulus we assume azimuthal symmetry and calculate the median value. As shown in Pingel et al. (2013), the median is a better representation of the average power because occasional bright pixels are present in the modulus image. They are caused by the Gibbs phenomenon. The Gibbs phenomenon (or the edge effect) results from image edges as galaxies are extended, and H I column densities never reach zero at the edges of the surveyed regions. As the Fourier transform of a step function is a sinc function (Bracewell 2006), bright pixels appear at the center of $P(k)$ (an example is shown in Figure 2 of Pingel et al. 2018). The median power is then plotted as a function of log (spatial scale), and the uncertainties are estimated using the median absolute deviation (MAD), e.g., Pingel et al. (2018).

In the SMC, it was found that a single power-law function fits the H I SPS well, $P(k) \propto k^{-\gamma}$ (Stanimirović et al. 1999; Stanimirović & Lazarian 2001). In the LMC, however, the SPS was best fit by a double power law, see Elmegreen et al. (2001), with the "break point" corresponding to a physical scale of $\sim$100 pc. To estimate the break point and the SPS slopes, in our fitting routine we iterate over all bins in the SPS (excluding 15% of the bins at the largest and smallest scales), and fit a double power law, with each bin being selected as the break point. We then calculate the χ^2 statistics and select as the best fit the break point that minimizes χ^2. We tested our fitting procedure on the H I column density subregions that were analyzed by Elmegreen et al. (2001) and also on the infrared 160 μm image from the *Spitzer Space Telescope* used in Block et al. (2010). In both analyses we found breaks, as well as SPS slopes, in agreement with results from those papers. This demonstrates that our fitting routine is reliable.

3.1.1. The Rolling SPS

In all previous studies a single or double power-law SPS slope was fit for the entire H I images of the SMC and LMC, or for several large subregions. Motivated by the improved spatial resolution of the ASKAP data, we investigate spatial variations of the SPS slope γ on much smaller scales than was previously done. To do this, we apply a rolling SPS method. We extract a square subimage of the H I column density image (850×850 pc for the SMC and 1.5×1.5 kpc for the LMC), and calculate γ at large and small scales along with the corresponding break point. We then shift the subimage by one beam width (10 pc for the SMC and 14.5 pc for the LMC) and repeat the procedure until the slope and the break point are calculated across the entire image. During the SPS fitting process, we take the average MAD value of a given bin across all subimages as the uniform weight given to that bin. We do this because the largest-scale bin sometimes has only a few data points, all with similar values, which gives that bin extremely large weight.

In addition, for each kernel for which we calculate the SPS, we test whether a single or a broken power law fits the SPS better in a statistically significant manner by employing the *F*-test (Snedecor & Cochran 1989). We estimate the goodness of fit for both models by the chi-squared statistic,

$$\chi^2 = \sum_{i}^{n} \frac{(Y_{\mathrm{obs},i} - Y_{\mathrm{calc},i})^2}{\sigma_i^2}, \tag{3}$$

where n is the number of bins in the SPS, $Y_{\mathrm{obs},i}$ is the observed power in a given bin, $Y_{\mathrm{calc},i}$ is the power according to the model, and σ_i^2 is the variance within the bin. The χ^2 values for the two models are then used to calculate the F-value,

$$F = \frac{(\chi_1^2 - \chi_2^2)/(p_2 - p_1)}{\chi_2^2/(n - p_2 - 1)}, \tag{4}$$

where subscripts 1 and 2 refer to the single and double power-law models, respectively, and p is the number of parameters in either model. At a significance level of 5%, a value F_{crit} can be calculated from an $F(p_2{-}p_1, n{-}p_2{-}1)$ distribution such that the null hypothesis of a single-slope fit is rejected if $F > F_{\mathrm{crit}}$ (Snedecor & Cochran 1989).

To test the validity and limitations of our rolling SPS method, we applied the same technique to simulated data with known γ. We simulated three images: two with a single input SPS slope of −2.7 and −3.7, and one with a double power-law SPS with large- and small-scale slopes of −2.7 and −3.7, respectively, with the break point at 130 pc (details on how simulated images are produced are given in Section 3.3). Our tests confirmed that the rolling SPS method successfully fits a double power law for the simulated image with two slopes, but clearly prefers a single power law for the other two simulated images. As shown in Figure 13 in the Appendix, the rolling SPS applied on the single-slope simulated images produced a mean γ that underestimated (causing the slope to become steeper) the input value by less than 10%, with a standard deviation of ∼0.2. The reason for this underestimation is the residual Gibbs phenomenon, which corrupts both large and small spatial scales but has a stronger effect on large spatial scales due to its $\sin(k)/k$ behavior. The standard deviation of the recovered slope values is a function of kernel size as the Gibbs effects becomes smaller when we use larger subimages. Increasing the kernel size past 1.5 kpc reduced the standard deviation of the slope values and brought the mean closer to the input value (as shown in Figure 14 in the Appendix). Ultimately, 1.5 kpc frames were deemed to produce acceptable results, as increasing the subimage size decreases the amount of usable pixels at the edge of the image and conveys less information about small-scale structural variations. Applying the rolling SPS to the simulated broken power-law image, mean small- and large-scale slopes in the image again slightly underestimated the input values, and the mean calculated break-point physical scale.

As a conclusion, our rolling SPS with the F-test distinguishes between single versus double power-law images. However, due to the residual Gibbs effect, it recovers slightly steeper slopes. As shown in our tests in the Appendix, this introduces a systematic uncertainty of ∼0.2 for our selected kernel size. However, this underestimate is still within 1σ of our SPS fitting uncertainty.

3.2. Structure Function

In addition to the SPS, we also use the SF to investigate turbulent properties of two-dimensional images (either brightness temperature or column density). At the start, we integrate the image over all velocity channels and then normalize the integrated image by its maximum pixel value. Because the SF is calculated in the image domain, it does not suffer from edge effects, which are commonly seen when an image is Fourier transformed. In addition, the image can have any size and shape. However, one disadvantage of the SF is that it covers a smaller range of spatial scales than the SPS.

We use Equation (5) to calculate the SF at each discrete pixel separation r, where r' represents any arbitrary pixel in the image and I represents either the normalized intensity or normalized column density of the pixel. For a given pixel separation r, there is a limited number of possible ways (or realizations) of selecting pixel pairs that can be calculated into the average squared difference of pixel intensities. We calculate SF SF_r for all realizations, and this allows us to estimate the mean SF_r and the standard deviation over different realizations. Next we bin r values by 0.05 pixels in log space. In doing so we use estimated uncertainties for each r to calculate the weighted average and standard deviation of a given bin. The bar Δv shows that the SF is calculated for a specific thickness of velocity channels. Throughout most of the paper we work with the column density images, and Δv is the full velocity range of a given spectral-line data cube (129 km s^{-1} in the case of the SMC ATCA + Parkes data cube, or 198 km s^{-1} in the case of the LMC ATCA + Parkes data cube). However, in Section 4.4 we investigate individual velocity channels, and there $\Delta v = 1.65$ km s^{-1}.

$$SF_r = \langle [I(r') - I(r' + r)]^2 \rangle_r |_{\Delta v}. \tag{5}$$

As with the SPS, we compute the rolling SF by calculating the SF slope for a small kernel and running the kernel across the whole image.

If the SPS of a 2D distribution is a power-law function with a spectral index γ (such that $P(k) \propto k^{-\gamma}$), then the SF will also be a power law with an index α, such that $SF(r) \propto r^{-\alpha}$. If $2 < \gamma < 4$, then the two indices are related by the equation (Simonetti et al. 1984)

$$\alpha = \gamma - 2. \tag{6}$$

However, the above relation between the SF and SPS is in practice an approximation. As explained by Hou et al. (1998), due to the limited image size and angular resolution, the SF can deviate from a simple power law on either small or larger spatial scale, complicating the selection for the range of spatial scales used to derive the slope. The level of deviation is a function of image size, resolution, and γ value, and it is difficult to predict analytically.

Figure 2 demonstrates the effect of divergence between the SPS and SF slopes. We use simulated images of 2D fractal Brownian motion (Section 3.3) to explore how the input power-law slope affects the shape of the SF to constrain the best spatial range for measuring the SF slope. We generated 100 simulated fBm images for SPS slope γ = –2 to −4 at 0.1 intervals, and for the image size of 255 × 255. In Figure 2 we show the relation between the true (input) SPS slope γ and the estimated SF slope (α). The top right panel shows the relation when the full range of data points is used for fitting α, while in the subsequent panels we use the middle 1/3, the first 1/3, and the last 1/3 of the spatial range for fitting, respectively. These figures show how much the measured α deviates from the relation given by Equation (6). For SPS slopes in the range −2.7 to −3.5, the range of slopes that is of interest when

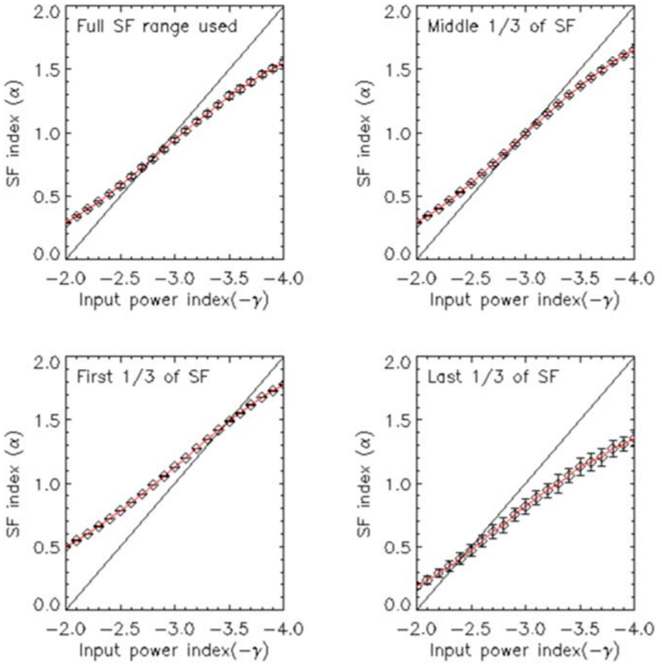

Figure 2. Comparison between the measured slopes of the structure function (SF) vs. the input spatial power spectrum slope. We generated 100 fBm images with the input SPS slope from −2 to −4 at 0.1 intervals. All images have a size of 255 by 255 pixels. The mean SF slope and standard deviation estimated for simulated images are plotted when the SF slope was calculated over the entire SF range (top left), the first 1/3 (bottom left), the middle 1/3 (top right), and the last 1/3 (bottom right) of the SF. The derived SF slope deviates from the true input SPS value. For the steep SPS slope (−3.5), measuring the first 1/3 of the SF range will produce the closest results. Conversely, if the SPS is shallow (−2.5), then the last 1/3 is a better range for measuring the SF slope. For SPS slopes in the range −2.7 to −3.5, the range using the central portion of the SF to calculate the slope is reasonable (within a few tenths of the actual SPS slope).

the SMC and LMC are studied, the middle 1/3 of the spatial range results in the SF slope that is within a few tenths of the actual slope expected based on the SPS slope. Based on these tests with simulated images, we conclude that when the SF slope is estimated using the middle 1/3 of the spatial fitting, the range is the most reasonable and accurate within±0.2 for the range of SPS slope from −2.2 to −3.8 (this range is of interest in our study based on previous SMC and LMC statistical investigations). Based on this, for our SF measurements in this paper we always fit using the middle third of the range of spatial scales provided.

3.3. Fractal Simulations

We performed simple 2D fractal Brownian motion (fBm) simulations to test the reliability of our measured SPS and SF slopes, as well as to estimate the degree of their statistical fluctuations. To generate simple (without noise) 2D fBm images (F), we use the prescription from Miville-Deschênes et al. (2003). We briefly summarize their approach here. To create an fBm-simulated image whose SPS follows a perfect power law (with random phase), we first start by generating a power-law isotropic amplitude (their Equation (3)),

$$A(\boldsymbol{k}) = A_0 k^{\gamma/2}. \tag{7}$$

Here, $\boldsymbol{k}$ is a 2D wavevector, whose length is the wavenumber k. A_0 is the normalization value and γ is the SPS slope. The phase $\phi(\mathbf{k})$ is randomly generated between -π and π, and additionally, we constrain $\phi(-\boldsymbol{k}) = -\phi(\boldsymbol{k})$ to ensure that the image in direct space is real. We now create the real and imaginary components of the Fourier transform,

$$\mathrm{Re}\,[F(\boldsymbol{k})] = A(\boldsymbol{k})\cos[\phi(\boldsymbol{k})], \tag{8}$$

$$\mathrm{Im}\,[F(\boldsymbol{k})] = A(\boldsymbol{k})\sin[\phi(\boldsymbol{k})]. \tag{9}$$

The Gaussian random field F (fBm) is the inverse Fourier transform of $F(\boldsymbol{k})$. Using this technique, we construct simulated images of various sizes and with the varying SPS slope.

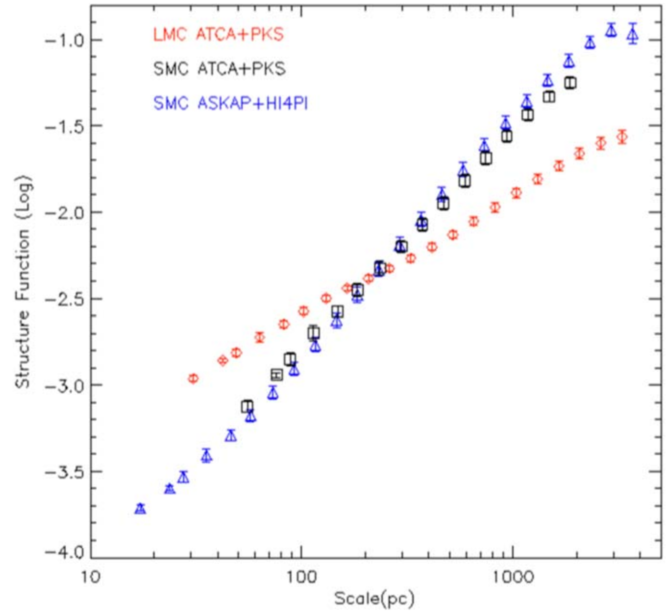

Figure 3. Global H I structure functions of the entire LMC and SMC H I integrated intensity images.

4. SMC SF and SPS Analysis

4.1. Global Properties

Figure 1 shows the H I integrated intensity image of the SMC obtained using ASKAP and HI4PI data. Although it was obtained with only 16 ASKAP antennas, the angular resolution of this image is already higher by a factor of three than the previous ATCA observations. In terms of sensitivity, the ATCA+Parkes data set is a factor of two more sensitive. The ASKAP image also has a slightly larger extent relative to the previous ATCA+Parkes image. The corresponding peak H I column density based on this image is in excellent agreement with that from Stanimirović et al. (1999).

Figure 3 shows global SFs calculated using the whole SMC and LMC H I column density images. For the SMC we show both the old ATCA + Parkes and the new ASKAP + HI4PI data sets to demonstrate how new H I observations have both higher spatial resolution and a slightly larger spatial coverage. The two SMC SFs agree well throughout most of the spatial range, with some small departures at the small and large ends. These SFs also show slight turnover at the largest spatial scales due to the effects we discussed in Section 3.2. In addition, this figure clearly shows that the SF slope of the LMC H I is significantly more shallow than the slope of the SMC. Finally, while the SMC SF is linear (in the log–log space), the LMC SF shows a break around 100–200 pc (we discuss this in Section 5). The break in

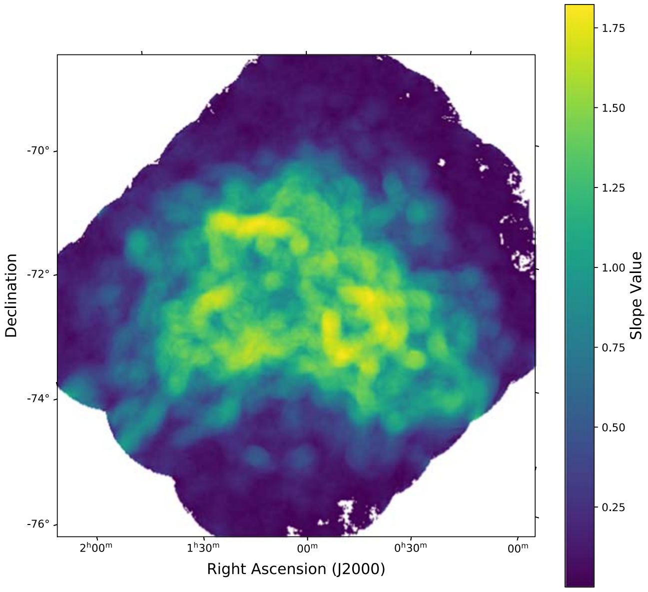

Figure 4. Image of the SMC structure function slope. We used a circular kernel of 51 pixels in diameter (corresponding to 24′) and applied the rolling SF calculation on the H I ASKAP+HI4PI integrated intensity image of the SMC. A small fraction of pixels with a slope value below 0, located in the far image outskirts, which are dominated by noise, have been removed. Motivated by previous studies, e.g., Stanimirović et al. (1999), a single power-law function was fit in each kernel. The effective angular resolution of this image is 24′. Based on our analysis with simulated data, the typical uncertainty of the SF slope is ∼0.2. While this image shows small spatial variations, they are consistent with statistical fluctuations and do not stand out as being statistically significant.

the SPS of the LMC has been found to be similar to the estimated H I scale height of ∼180 pc (Kim et al. 1998). The lack of a break in the SPS of the SMC can be explained as being due to the lack of a "thin disk." Indeed, Stanimirović et al. (2004) provided a rough estimate of the H I scale height of 1 kpc based on the typical size of large H I shells as well as on the velocity dispersion.

4.2. Spatial Distribution of the SMC H I SF and SPS Slopes

We next run a circular kernel with a diameter of 51 pixels (corresponding to ∼24′ and covering the spatial range 8–415 pc) across the SMC H I integrated intensity image from ASKAP + HI4PI and in each kernel calculate the SF. For each SF we fit a single power-law function (based on previous studies) and map out the estimated slope spatially across the SMC.

The resulting image of the SF slope is shown in Figure 4 and has a resolution of 24′. The SF slope ranges between ∼1.0 and 1.6. When we apply our arguments from Section 3.2, this range corresponds to the SPS slope −3.0 to −3.6. While the image shows small spatial variations, they are not significant and are consistent with statistical fluctuations, as shown in Figure 5. In Figure 5 we show the histogram of SF slopes for the SMC image and 100 simulated images. We generated 100 fBm images all with an input SPS slope of −3.4. We then treated each simulated image like observations and calculated the rolling SF slope. The histogram of all SF slopes is shown in solid blue. When the SMC signal-to-noise ratio (S/N) $S/N > 5$ pixels are considered (dotted green line), the simulated SF slope agrees well with observations. This demonstrates that for the same SPS slope, statistical fluctuations

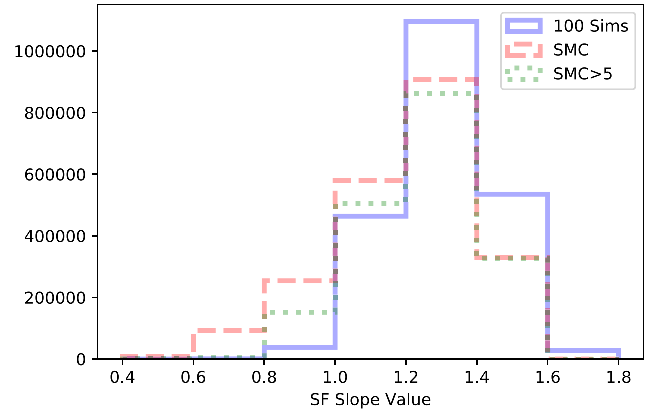

Figure 5. The histogram of the SMC SF slope (with a bin spacing of 0.2) showing data from Figure 4 (red) and after excluding pixels with $S/N < 5$ (green). The histogram of SF slopes for the 100 simulated images, generated to have an SPS slope of −3.4, is shown in blue.

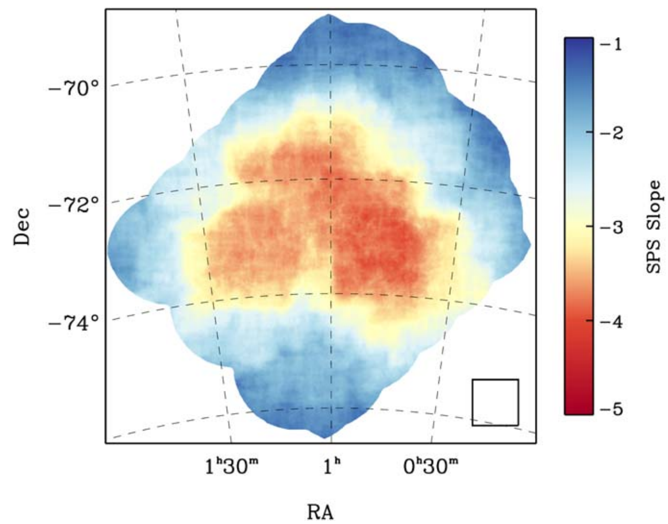

Figure 6. The SPS slope image calculated from the SMC H I (ASKAP+HI4PI) integrated intensity image. Each pixel represents the center of an 850 pc square kernel, shown in the lower right corner, in which the SPS was calculated. A single power-law function was fit in each kernel. The effective angular resolution of this image is ∼49′. The typical uncertainty of the SPS slope per kernel is 0.1–0.3.

will result in a small range of SFs—this range is consistent with what we find across the SMC. This exercise also shows that the typical uncertainty of our calculated SF slopes is ±0.2 (estimated as the standard deviation of the simulated distribution), in agreement with our considerations in Section 3.2.

We obtain a very similar result when we apply the rolling SPS and calculate the spatial distribution of the SPS slope, shown in Figure 6. To compute this image, we use a kernel size of 850 pc and shift by 8 pc (the pixel size of the H I integrated intensity image). We fit a single slope based on previous studies, and also after investigating SFs of various subregions. In addition, we also allowed for fitting a double power law and used the F-test to decide which of the two models fit the data better. We found that for some pixels the *F*-test preferred a double power law. Despite this, the probability distributions of single, large-scale, and small-scale slopes across the galaxy all peak near the same value, a characteristic that is also present in single-slope simulated images. The rolling SPS image (shown in Figure 6) has a median slope of -3.0 ± 0.5 (error estimated by MAD) and a mean slope of -3.0 ± 0.6 within the region studied by Stanimirović & Lazarian (2001). These values are in agreement with their SPS slope calculation of -3.3 ± 0.01 using the entire H I column density image. The median fitting uncertainty across all kernels is 0.15.

The SF and SPS slope images suggest highly uniform turbulent properties for the H I in the SMC. This is a surprising result considering the SMC–LMC–MW interactions, where being the lowest mass, the SMC has suffered significantly and much of the SMC H I has been pulled out to form the Bridge and the Stream. Our estimated slope values and their range are in agreement with previous studies, e.g., Stanimirović et al. (1999), Stanimirović & Lazarian (2001), and Nestingen-Palm et al. (2017).

4.3. Correlations with the SFR and Stellar Surface Densities

Figure 7 shows the slope and normalization of the rolling SF calculated using the SMC H I integrated intensity image, overlaid with the SFR surface density contours (smoothed to the same resolution). Numerical simulations (e.g., Walker et al. 2014; Grisdale et al. 2017) suggest that stellar feedback steepens the SPS or SF slope by destroying clouds and shifting the power from small to large spatial scales. We would therefore expect to see a larger SF slope at the position of sites of recent star formation. However, in the SMC we do not find any obvious correlation between the SFR surface density and the SF slope or the normalization value. Similarly, we do not find that distributions of either the SF slope or the normalization value correlate with the stellar surface density.

4.4. Probing Velocity Fluctuations

Numerical simulations of stellar winds by Offner & Arce (2015) have suggested that stellar winds can significantly influence the velocity power spectrum, while the density power spectrum can be less affected. We have so far considered only fluctuations in the H I integrated intensity images. Lazarian & Pogosyan (2000) suggested that the SPS of integrated intensity images probes density fluctuations, while velocity fluctuations are more prominent when intensity fluctuations of individual velocity channels are examined. In addition, as velocity fluctuations can contribute to intensity fluctuations, the SPS slope of individual velocity channels is expected to be more shallow than the slope of the integrated intensity image. Stanimirović & Lazarian (2001) investigated the SPS of the entire SMC ATCA + Parkes data set and showed that the SPS slope of the entire SMC calculated for a velocity thickness of $\Delta v = 1.65\ \mathrm{km\ s^{-1}}$ is indeed more shallow than the slope of the entire integrated intensity image (2.8 versus 3.3). We now investigate the spatial variability of the SF slope at $\Delta v = 1.65\ \mathrm{km\ s^{-1}}$.

For each individual velocity channel in the emission-dominated velocity range 110–210 $\mathrm{km\ s^{-1}}$ (60 channels in total), we calculate the SF. We can do this using two different approaches. First, for each of the 60 velocity channels we calculate the SF using Equation (5), and then we average all 60 SFs. The result is shown in Figure 8 using red triangles. Second, for each individual velocity channel, we run the rolling SF method and calculate the SF in each 51-pixel-wide kernel (this results in 776,520 kernels $\times$ 60 channels $= 4.7 \times 10^7$ individual SFs), and then we average all SFs. The resulting SF

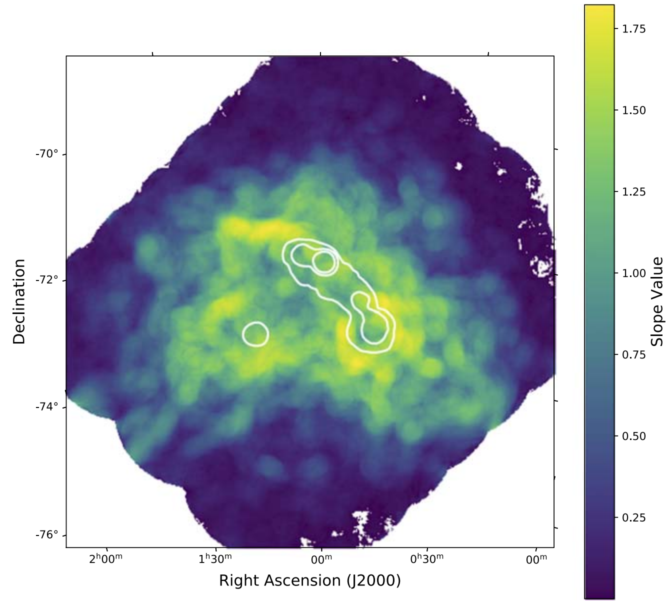

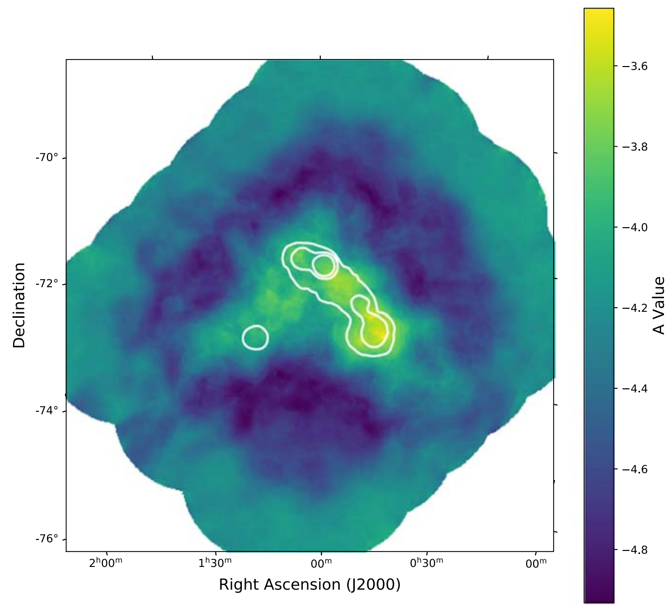

Figure 7. (Top) The rolling SF slope of the SMC H I integrated intensity image obtained from the ASKAP+HI4PI data, following Figure 4. The SFR surface density is overlaid with contours at 0.005, 0.012, and 0.024 MJy $\mathrm{sr^{-1}}$. (Bottom) The normalization value of the fitted SF power-law functions overlaid with the SFR surface density.

is shown with yellow right-hand triangles in Figure 8. These two SFs are in excellent agreement for the overlapping range of spatial scales.

As a comparison, in the same figure we show SFs for the velocity-integrated H I image (with $\Delta v = 129\ \mathrm{km\ s^{-1}}$). Again, we can calculate this using the two different methods. First, the blue squares show the SF calculated using the whole SMC velocity-integrated intensity H I image. This is the same SF as we show in Figure 3 (blue triangles). Second, using the rolling SF method, we can calculate the SF for 776,520 kernels in the H I integrated intensity image. The average of these SFs is shown with green diamonds. Again, the two SFs are in excellent agreement over the overlapping range of scales.

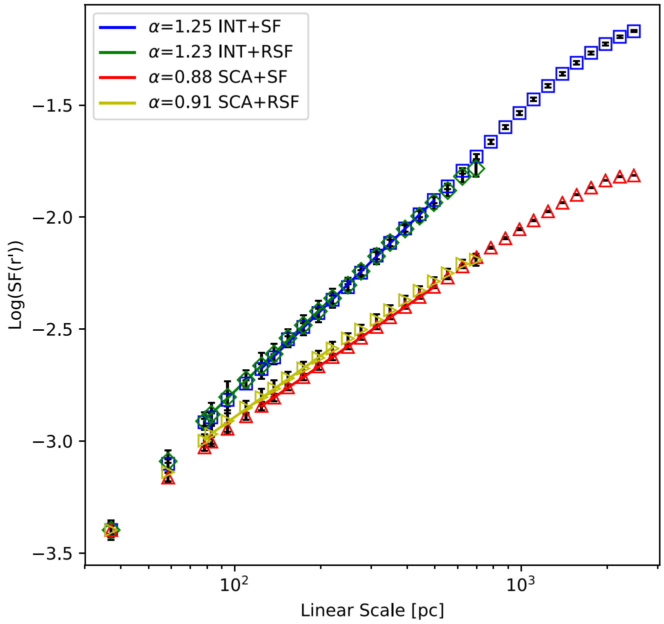

Figure 8. SMC structure functions: SF of the H I velocity-integrated intensity image (squares), rolling SF average of the H I velocity-integrated intensity image (diamonds), average SF of the individual velocity channels (110 to 210 km s^{-1} range, triangles), and an average of the rolling SF averages of the individual velocity channels (right-hand triangles). We have normalized all SFs at ∼25 pc by subtracting the difference of their first bin from all bins.

However, it is obvious that the SFs of the integrated intensity image have a steeper slope than the SFs of individual velocity channels, in agreement with expectations from Lazarian & Pogosyan (2000). This result agrees with previous studies, e.g., Stanimirović & Lazarian (2001) and Nestingen-Palm et al. (2017). While this is not a new result, we have shown that calculating rolling SFs produces consistent results (when compared over the same range of spatial scales) to more traditional approaches of using an entire image. We have also compared the SF slope images calculated for individual velocity channels with the SFR surface density, but did not find any obvious correlations.

5. LMC Statistical Analysis

5.1. Global Properties

As shown in Figure 3, the SF slope of the LMC H I is more shallow than the slope of the SMC. In addition, while the SMC SF is linear (in the log–log space), the LMC SF has a likely break around 100–200 pc, which is even more pronounced when the SFs of more localized regions are examined. In Figure 9 (top) we show four selected regions that display significant variability of the SFs within the LMC. The SF for these four regions are shown in Figure 9 (bottom). The four areas include 30 Dor, the center of the LMC, and two positions in the outskirts of the LMC. This figure shows not only that SFs change significantly across the LMC, but that multiple breaks likely exist.

The influence of the LMC disk on the SPS has been noted in several studies. In addition to Elmegreen et al. (2001) and Padoan et al. (2001), Block et al. (2010) more recently used *Spitzer* IR images at several wavelengths, 24, 70, and 100 μm, and showed a clear break at a spatial scale of 100–200 pc. As we discussed in Section 3.2, the SF suffers at both small and large spatial scales due to the limited image resolution and size.

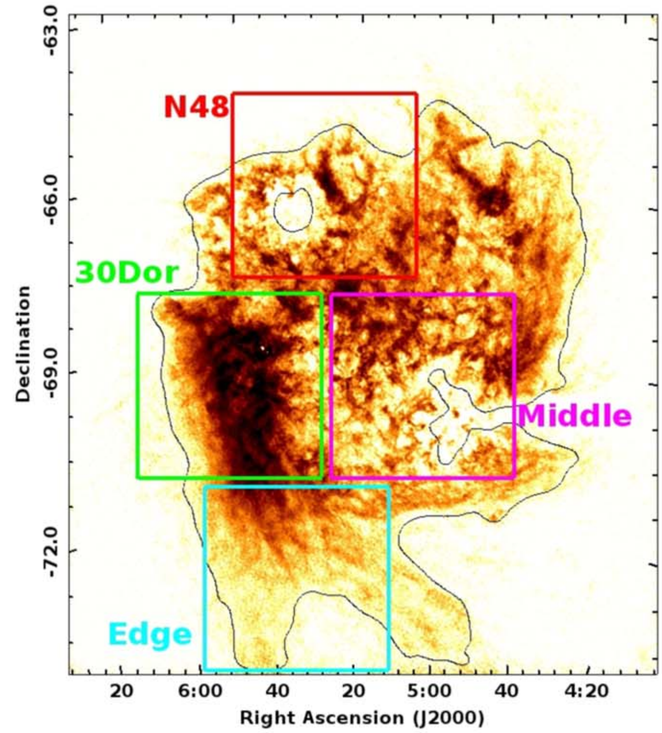

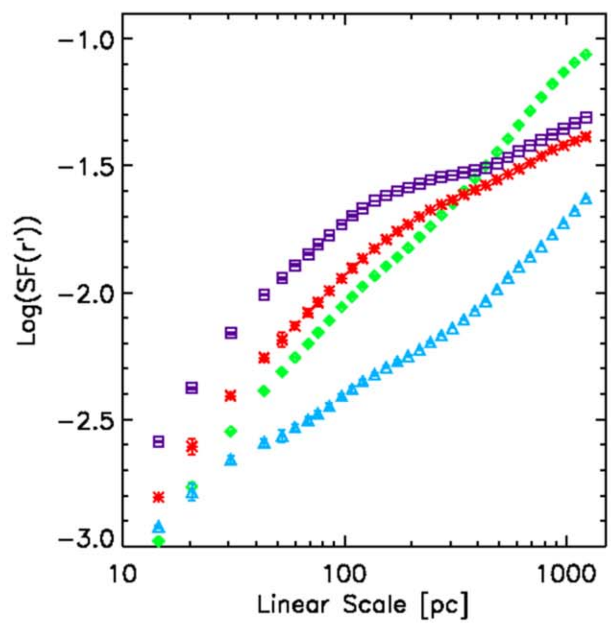

Figure 9. (top) The H I integrated intensity image of the LMC with four selected regions: a region around the star-forming region N48 (red), 30 Doradus (green), roughly the middle area of the LMC (magenta), and the bottom edge of the LMC (cyan). All areas are square and 2.8 kpc across. The black contour line shows where the intensity is 3σ above the noise level. (Bottom) SFs of the four LMC regions (red asterisks, green diamonds, magenta squares, and cyan triangles). Uncertainties are typically smaller than the symbol sizes.

Adding further complexities caused by the presence of a prominent disk-like structure would introduce further deviations and complicate the interpretation of SFs slopes and possible breaks even more. Because of this, when we investigate spatial variations of turbulent properties across the LMC, we use only the SPS.

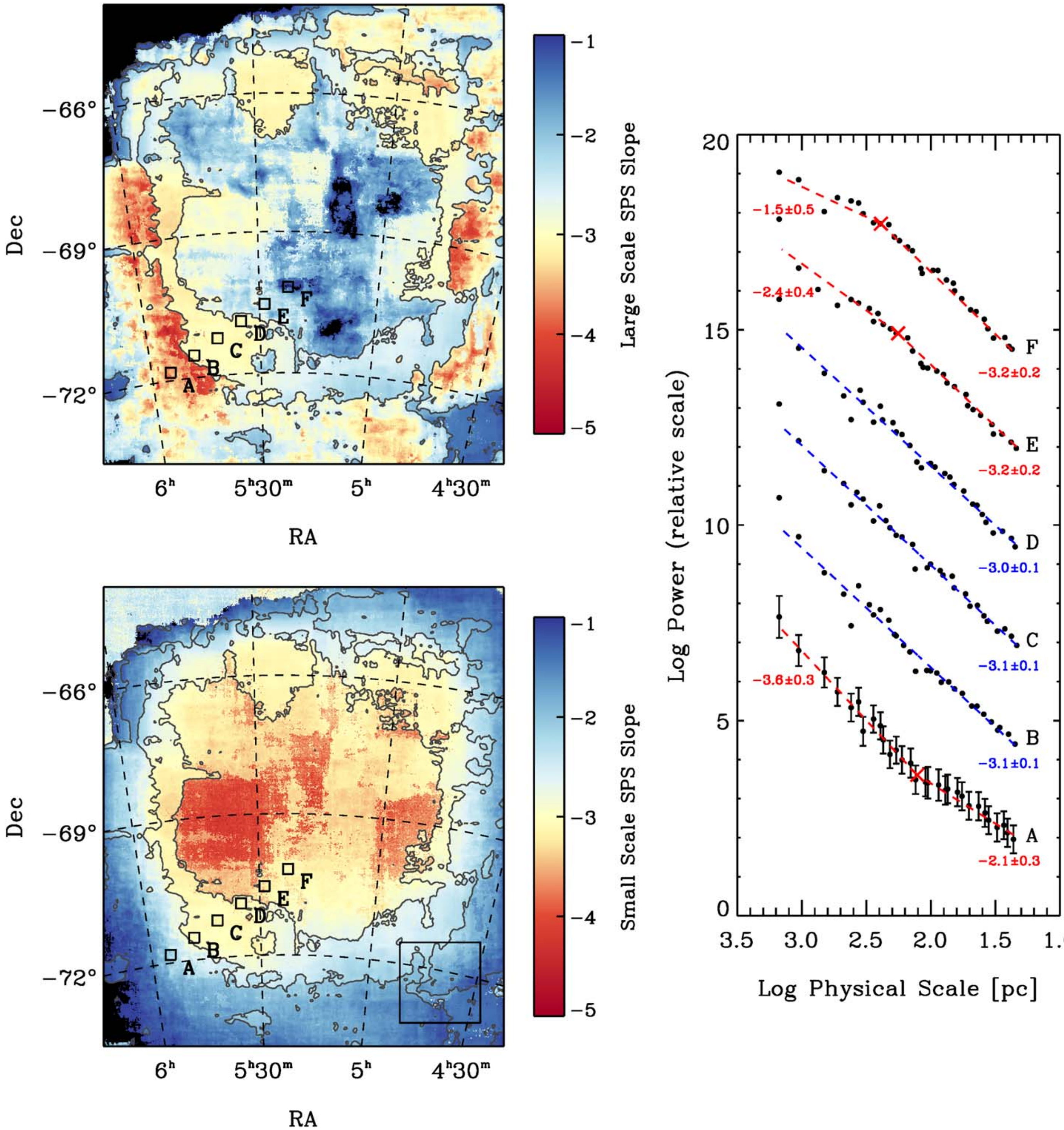

Figure 10. (Top left) Large-scale SPS slope for the LMC H I column density image. Each pixel represents the center of a 1500 × 1500 pc kernel in which the slope was calculated. Contours enclose regions in which a single power-law model better fits the data at a 5% significance level, and where slopes from this simpler model are plotted. Black pixels indicate fitted slopes outside the color-bar range. (Bottom left) Small-scale SPS slope across the LMC, including a box in the bottom right corner indicating the kernel size. The median fitting uncertainty for estimated slopes on both small and large scales is about 0.2–0.4. (Right) Relative SPS averaged over 121 kernels centered within the squares shown in the images. SPSs are fit with a broken power law where applicable, shown as red dashed lines, and with a single power law shown in blue where the *F*-test signals a failure to reject the simpler model. Slope values and one-sigma uncertainties are displayed at corresponding ends of the spectra along with red crosses at the detected break points. Error bars are identical in each spectrum, as prescribed in Section 3.1.

5.2. Spatial Distribution of the LMC H I SPS Slope

We apply the rolling SPS method on the H I integrated intensity image of the LMC. For each kernel where we calculate the SPS, we test whether a single or a broken power-law fits the SPS better in a statistically significant manner by employing the *F*-test (see Section 3.1.1). The large- and small-scale slope distributions across the LMC are shown in Figure 10, and the corresponding physical scales of the break points are plotted in

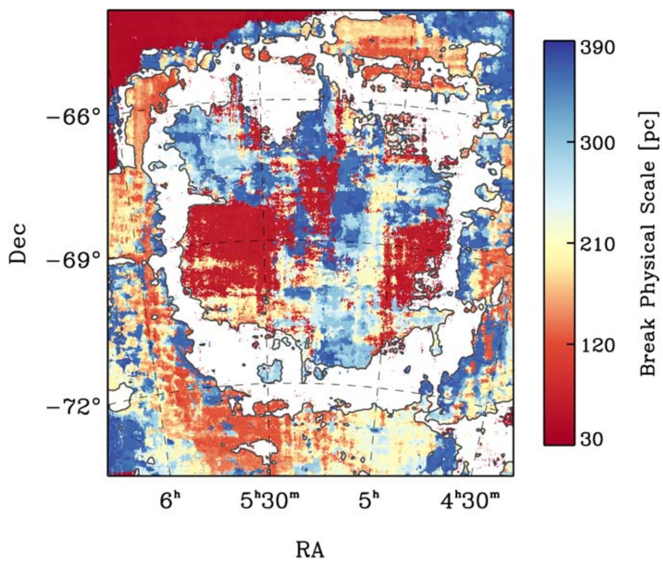

Figure 11. Physical scale corresponding to the break point in the LMC SPS. The rolling SPS samples scales from 15 to 1500 pc, but 15% of the bins are discarded at each extreme, leaving potential break points between 34 and 415 pc. Black contours enclose white pixels where a single power-law model better fits the data at a 5% significance level.

Figure 11. Contours enclose regions where we fail to reject the null hypothesis, i.e., where a single power-law model is a more appropriate fit. The single power-law fit is preferred primarily in an annular region and for 30.0% of pixels. The median fitting uncertainty for estimated slopes is 0.2 for a single power-law fit, and 0.2–0.4 for the large- and small-scale slopes, respectively. We also show in Figure 10 several example spatial power spectra obtained at representative positions A-F. Each shown SPS was obtained by averaging the SPS calculated for 121 individual kernels all centered near a particular position.

In agreement with previous studies, e.g., Elmegreen et al. (2001), Padoan et al. (2001), and Block et al. (2010), we find that most of the LMC requires a broken power law to fit the SPS. For most of the LMC area, the large spatial scales have a more shallow SPS slope, >-3 versus <-3, at small scales. This is in agreement with previous studies (e.g., Elmegreen et al. 2001; Block et al. 2010) where the central portion of the LMC H I distribution is dominated by the disk and 2D turbulence, which results in a shallow SPS slope (difference from ~ -3.7 to ~ -2.2).

Interestingly, on small spatial scales we find localized regions with very steep slope (<-4). The most prominent is the 30Dor region, and other regions are close to well-known H II regions: N48, N11, and N79. This is in agreement with predictions from numerical simulations for the influence of the stellar feedback and localized steepening of the SPS slope (Grisdale et al. 2017, 2019). Stellar feedback via supernovae and stellar winds removes gas from clouds or totally destroys clouds, effectively shifting power from small to large spatial scales. Considering our typical fitting uncertainty (0.2–0.4), the difference between very steep slopes (~ -3.9) caused by stellar feedback relative to the surroundings (slope of ~ -3) is clear.

While throughout most of the LMC on large scales the SPS slope is >-3, at the extreme LMC outskirts the slope becomes steep, reaching values <-3.8 in two extended elongated regions. Again, this change clearly stands out even when the uncertainties associated with the rolling SPS derivation are taken into account. We are confident that these steep slope regions are not caused by artifacts or image edges because we find them only in the LMC. Any artifacts caused by the fast Fourier transform (FFT) or our kernel size should affect the SMC and the LMC equally because kernels in either analysis span the same number of image pixels. In addition, as shown in Figure 10 (right), the SPS slope change is gradual and not random. Pointings F to A demonstrate how the SPS changes its shape and slopes from the center to the outskirts. While at pointing A the SPS essentially has a convex shape, by pointing F, this has flipped into a concave shape.

These elongated regions with a very steep large-scale slope are at the edges or just beyond the stellar disk. On the southwest side, the steep SPS slope is in the region where optical observations have discovered warping and flaring of the stellar disk (Olsen & Salyk 2002; Choi et al. 2018). The steepening of the SPS slope we find likely indicates the transition from 2D to 3D turbulence due the presence of the H I disk flaring and a rapid increase in the disk scale height. While within the thin H I disk turbulence is dominated by 2D motions, within the H I flare the disk thickness increases, resulting in 3D turbulent motions.

On the southeast side of the disk, we see similar steepening in the region at the edge of the stellar disk and right at the position of the "leading H I edge." One possible explanation is that we see the southeast flare of the H I disk, just like on the southwest side. While this has not been seen previously, it was predicted in Besla et al. (2012) that stellar and gaseous disks are both warped and flared. In addition to the extended region of steep SPS slope, there is an indication that at this side of the disk, the SPS slope has a more fragmented and patchy distribution. This might be caused by the ram-pressure effects because the LMC disk interacts with the hot MW halo.

The image of the SPS break points shows interesting spatial variations. We emphasize that both low and high extremes of the break-point range are not well constrained with our fitting. The localized areas around 30Dor, N48, N11, and N79 seem to indicate the lowest disk thickness, <50 pc. The central regions of the LMC have a slightly higher thickness $\sim$200–300 pc. The elongated regions in the outskirts with steep SPS slope have a thickness of $>$150–400 pc. Most previous studies of the LMC have found a break at about 200 pc, in agreement with the estimate of the H I disk thickness of about 180 pc (Kim et al. 1998).

5.3. Correlations with the SFR and Stellar Surface Densities

Figure 12 shows the large- and small-scale SPS slopes overlaid with the SFR surface density and the stellar surface density (provided by the 3.6 μm *Spitzer* image). The SFR and stellar surface densities were smoothed to the resolution of the SPS slope images. With the coarse resolution of the SPS slope images, we can see that the 30 Doradus region overlaps with the localized region where the small-scale SPS slope is very steep. Similarly, positions of N79 and N11 coincide with locations where the small-scale SPS slope is steep. In particular, N79 has recently been classified as a super star cluster candidate and is known to contain powerful outflows and an H II region (Nayak et al. 2019).

The elongated regions with a steep slope that appear in the large-scale SPS slope image are positioned right at the edges of the SFR surface density contours. On the northeast side (where the H I leading edge is), the elongated region of very steep

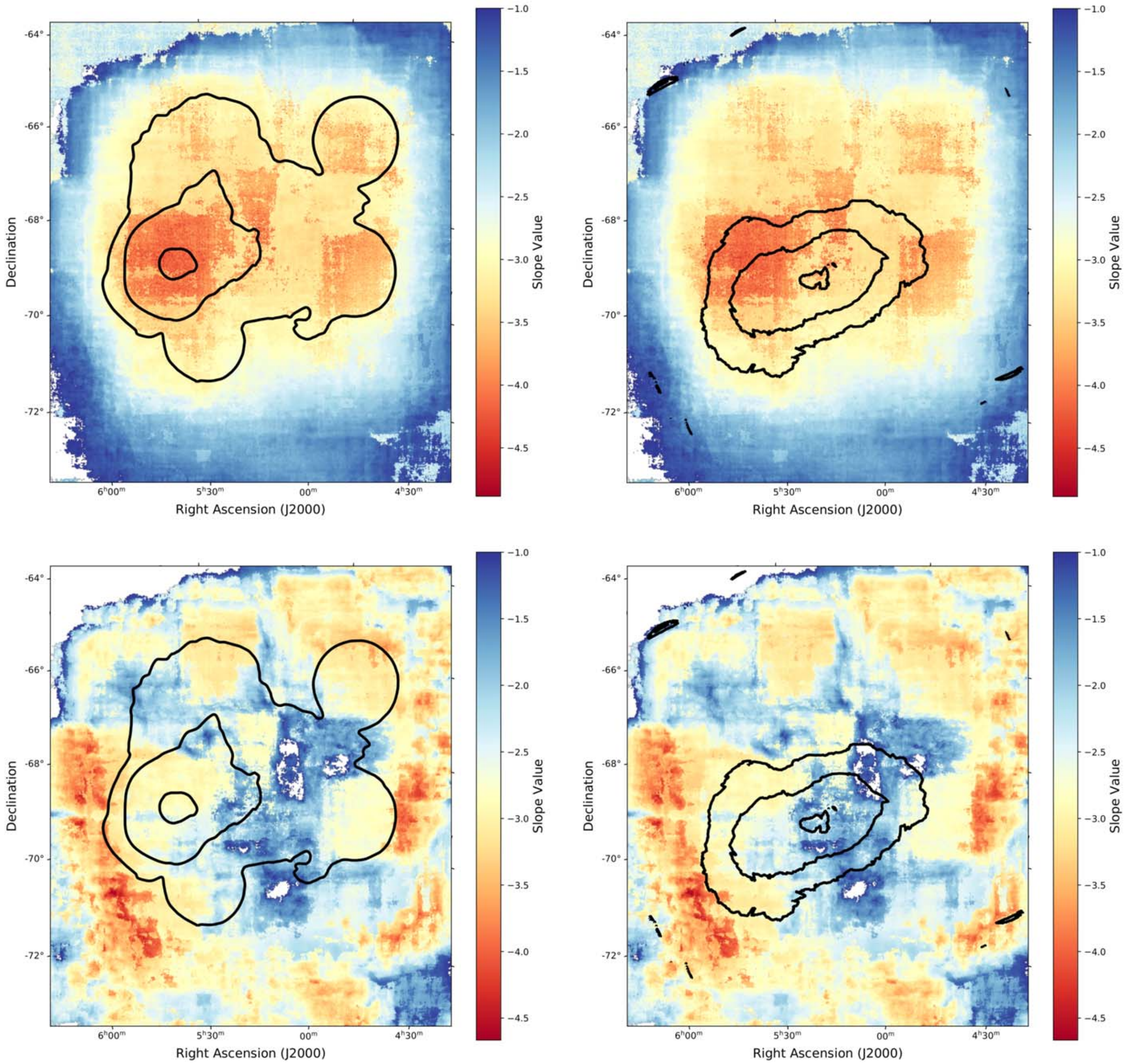

Figure 12. (Upper left) Map of the small-scale SPS slope γ across the integrated LMC image overlaid with the SFR surface density. (Upper right) Map of the small-scale SPS slope γ across the integrated LMC image overlaid with the stellar surface density. (Lower left) Map of the large-scale SPS slope γ across the integrated LMC image overlaid with the SFR surface density. (Lower left) Map of the large-scale SPS slope γ across the integrated LMC image overlaid with the stellar surface density. The SFR surface density contours are shown at 0.0022, 0.009, and 0.095 MJy sr^{-1}. The stellar surface density contours are at 0.25, 0.41, and 0.6 MJy sr^{-1}.

slope coincides with the edge of the stellar disk, while on the southwest side, the elongated region with the steep slope is located beyond the stellar disk. This is in agreement with the H I distribution and also with the 160 μm *Spitzer* image, which traces large dust grains that are well mixed with H I. On the northeast side, the stellar distribution extends all the way to edge of the leading edge (seen in H I and 160 μm), while on the southwest side, gas and large dust grains have a more extended distribution relative to the stars. Generally, the stellar contours occupy the region of the shallow large-scale SPS slope (>-3).

In summary, the small-scale SPS slope shows a clear correlation with several most prominent H II regions, in agreement with what is expected due to stellar feedback, the SPS slope becoming very steep as supernovae, stellar winds, and outflows disrupt and destroy interstellar clouds. The large-scale SPS slope image has the most shallow SPS slope, roughly in agreement with the extent of the stellar disk. The two elongated regions in the disk outskirts with a very steep slope are both located just beyond the stellar and star-forming disk of the LMC.

6. Discussion

We developed methods for mapping spatial variations of the SPS and SF slope for the first time, with the goal of connecting H I statistical properties with the underlying turbulent drivers.

With future high-resolution H I observations, these methods can be applied to many other galaxies. A high spatial resolution, so that we can reach the scales of stellar feedback sources (e.g., individual H II regions and SNe), as well as a high spatial dynamic range are needed for mapping out spatial variations of interstellar turbulence. With the upcoming new radio telescopes ASKAP, MeerKAT, and the SKA, such data sets will become increasingly more available.

6.1. The SMC

In the case of the SMC, we find highly uniform turbulent properties of H I. We have employed the rolling SPS, the rolling SF, and also investigated individual velocity channels, where based on Offner & Arce (2015), turbulent properties should be more pronounced. However, we do not find evidence for local enhancements of turbulence due to stellar feedback. A similar conclusion was reached in Nestingen-Palm et al. (2017), who investigated turbulent properties within the central star-forming SMC versus outer SMC regions and did not find any difference. Nestingen-Palm et al. (2017) showed that this lack of difference of turbulent properties cannot be explained by the high optical depth H I, and that it is most likely due to a significant turbulent driving on large scales. Numerical simulations by Yoo & Cho (2014) showed that the turbulent energy spectrum is very sensitive to large-scale driving. Unless the energy injection rates on small scales are much higher than the energy injection rate on large scales, the large-scale driving will always dominate.

Alternatively, we may be probing incorrect modes of turbulence. For example, several studies have shown that mechanical feedback from stellar winds is reduced in low-metallicity environments (Ramachandran et al. 2019). Therefore, supernova-driven turbulence could be more pronounced in the SMC than the LMC or the MW. Orkisz et al. (2017) showed that in the case of Orion star-forming region, most of the cloud motions are solenoidal, while around main star-forming regions, the motions are driven by compressive turbulent forcing. As proposed by Federrath & Klessen (2012), the supernova-driven turbulence is likely to be more effective in producing compressive motions. Therefore it is an important future task to perform a statistical analysis that can separate solenoidal from compressive motions.

Finally, the SMC is known to have a large line-of-sight depth, e.g., Mackey et al. (2018). It is therefore possible that effects of stellar feedback, which are localized in space and velocity, may simply become quickly washed out when the integration is performed over a very long line of sight. To roughly test this hypothesis, we have used our fBm simulations to create a random image with an SPS slope of -3.4. We then inserted into this image a smaller subregion, having simulated a much steeper slope of -4.0 to effectively mimic the localized effect of stellar feedback. The subimage had smoothed edges in order to blend well and not cause significant Gibbs ringing. We have then generated several additional images with only a slope of -3.4 and added all images together to effectively simulate a longer line of sight of the SMC. This experiment showed that adding only two to three images was able to wash out the spatial evidence of stellar feedback. While this is not a conclusive experiment and does not simulate velocity fluctuations produced by stellar feedback, it demonstrates that a significant line-of-sight depth could mask out localized regions with a steeper SPS slope.

6.2. The LMC

In contrast to the SMC, the LMC H I shows a complex diversity in terms of its turbulent properties. We find that across most of the LMC, the small-scale slope is steeper than the large-scale slope. The break in the SPS of the LMC H I data from Kim et al. (1998) has first been noted by Elmegreen et al. (2001), who found a slight steepening in the SPS on scales smaller than ∼100 pc and suggested that this could mark the transition from H I emission that comes from a relatively thinner line of sight to that corresponding to the thicker line of sight. This line-of-sight depth change is caused by the change in the depth of the H I layer due to the disk structure of the LMC. In Elmegreen et al. (2001), the SPS slope on small scales was steep, about -3.7, but flattened on scales >100–200 pc to about -2.7. Using 100 μm *Spitzer* observations of the LMC, Block et al. (2010) noted a change in SPS slope from -3.1 on scales <100–200 pc, to -2.1 on larger scales. Bournaud et al. (2010) simulated an LMC-sized galaxy and reproduced the double power-law SPS of the H I column density. They found a power law on large scales with a slope of -1.9, while on small scales, the slope was -3.1. On scales smaller than the disk scale height, the gas density has a density power spectrum as would be expected for a 3D turbulence. The motions corresponding to the large scales are quasi-2D and highly anisotropic. The SPS slopes we find are in agreement with the Bournaud et al. (2010) simulations, as well as previous H I and infrared studies.

6.2.1. Influence of Stellar Feedback

However, relative to previous studies, we also find significant localized changes in the SPS slope. On small spatial scales, we find several areas of localized steepening of the SPS slope around major H II regions. The most prominent is the 30 Doradus region, where the small-scale SPS slope changes from ~-3 to ~-4. This is in agreement with predictions from numerical simulations, e.g., Walker et al. (2014) and Grisdale et al. (2017), where stellar feedback erodes and destroys small clouds, and effectively shifts power from small to large scales. This is the first direct observational evidence of localized modifications of the SPS caused by stellar feedback. In the Grisdale et al. (2017) simulations, stellar feedback affects the nature of turbulence by increasing the fraction of energy in compressive turbulent modes (via supernovae and H II region expansion and heating). We note that the H I column density image of the LMC used in our study was not corrected for the high optical depth because H I absorption spectra in the direction of the LMC are currently not available (this will be possible in the near future, especially with the upcoming ASKAP observations).

6.2.2. Flaring of the LMC H I Disk

We also find localized large-scale steepening of the SPS slope in the outskirts of the LMC. We suggest that this is likely due to flaring of the H I disk and the increase of the H I thickness that causes transitions from 2D to 3D turbulence. Alternatively, the SPS steepening could be caused by the ram-pressure stripping on the southeast side and/or by magnetorotational instability, which has been proposed to be important for driving turbulence in the outer regions of galaxies (Piontek & Ostriker 2005). While H I observational studies of the LMC have so far failed to detect flaring of the H I disk, numerical simulations have suggested that both stellar and gas disks should be significantly warped and flared due to gravitational interactions with the SMC. Besla et al. (2012) performed numerical simulations of the SMC–LMC interactions with the goal of reproducing large-scale H I and the stellar structure of the Magellanic System. In their models they found that the outer LMC stellar and gas disks are significantly warped and distorted. Their figures show significant warp of the gas disk on one side, due to interactions with the SMC, while on both sides, the disk appears flared at about 5–6 kpc away from the center (roughly at about 6° from the center).

The stellar LMC disk has been observed to be both warped and flared (Alves & Nelson 2000; van der Marel & Cioni 2001; Olsen & Salyk 2002; Nikolaev et al. 2004). By observing red clump stars in 50 randomly selected fields in the LMC, Olsen & Salyk (2002) found that fields at the southwestern edge fall systematically low when compared with the fitted plane, and the authors concluded that the most likely explanation is the existence of a stellar warp. They suggested that the warp begins at a radius ∼3° from the LMC center, is about 2 kpc wide, and lies out of the plane by ∼2.5 kpc. More recently, using the Dark Energy Camera, Mackey et al. (2018) discovered that the outer LMC stellar disk is significantly truncated both on the west and south (the side closest to the SMC) side, and is extended in the north. The north–south orientation of the outer disk is different from that of the inner disk, in agreement with the expectations if the disk is warped.

In the MW H I disk, the locations of the H I warp and flare roughly coincide (Levine et al. 2006). The steepening of the SPS slope we find in the southwest appears roughly in agreement (in terms of both position and extent) with the Olsen & Salyk (2002) warp. Therefore, we conclude that the SPS slope change is most likely caused by the transition from 2D to 3D turbulence due the increase of the H I disk thickness starting at the position of the stellar warp. Although not well constrained by our fitting, the break-point map suggests an H I thickness >150 pc in this region.

Based on recent proper motion measurements, it appears that the complex morphology of the LMC disk is heavily influenced by interactions with the SMC. Choi et al. (2018) used ∼2.2 million red clump stars from the Survey of the MAgellanic Stellar History to examine LMC stellar disk structure. They reproduced the Olsen & Salyk (2002) inner warp in the southwest. Thanks to their large spatial coverage, they also discovered a new prominent warp in the southwest that is located about 7° from the center and departs from the fitted disk plane by ∼4 kpc. Because Besla et al. (2012) predicted in one of their simulations (Model 2) outer warps both in stellar and gaseous disks, Choi et al. concluded that their warp is in agreement with predictions from simulations for the scenario of a recent direct collision between the SMC and LMC. The Choi et al. warp is beyond the extent of the current H I data and remains to be examined in the future.

The H I disk of the LMC has been known to have an elongated region in the southeast that is aligned with the border of the optical disk. The region shows a steep increase in the H I column density distribution (Putman et al. 2003; Staveley-Smith et al. 2003). Because the LMC proper motion vector is directed to the east, it has been suggested that this high-density region was caused by ram pressure acting on the leading edge of the LMC disk and is therefore due to interactions with the hot MW halo. Mastropietro et al. (2009) simulated the interaction between the MW halo and the LMC gaseous disk and showed that a gaseous disk becomes strongly asymmetric with a compression at the front edge, in agreement with what is seen in H I. In their simulations, the high-density region is well defined and localized within 1.5 kpc from the disk border. In addition, they find that the average thickness and velocity dispersion along the line of sight are larger in this feature than in the rest of the disk. Salem et al. (2015) simulated the implications of ram pressure on the LMC H I and showed that simulations can match the observed leading edge if the MW halo density is $\sim10^{-4}$ cm^{-3}. The elongated area of steep large-scale SPS slope we find in the southeast coincides with the leading H I edge, where significant ram-pressure effects are expected. With the current data we cannot distinguish whether this steep slope area traces the flaring of the H I disk or a shock-like turbulence induced by ram pressure. Higher resolution and larger area images of the LMC in the future would allow us to map the SPS slope further beyond the stellar disk and properly fit the SPS slope break associated with the H I flare, therefore distinguishing between the two scenarios.

6.2.3. The LMC Disk Thickness

Padoan et al. (2001) used the spectral correlation function to map out the spatial distribution of the H I scale height in the LMC. They found that the scale height varies from 130 to 280 pc, with the largest scale height being found around 30 Doradus. Their average H I scale height was in excellent agreement with Kim et al. (1998), who used the H I velocity dispersion to estimate a scale height of ∼180 pc. Interestingly, Padoan et al. (2001) also mentioned that on spatial scales of a few hundred parsec, they sometimes found another possible change in the spectral correlation function and suggested that this may be caused by the effects of differential rotation. Throughout the LMC, we find that the disk thickness ranges from ∼50 to ∼400 pc. 30 Doradus has the lowest disk thickness, while the elongated regions in the LMC outskirts have a disk thickness of >150 pc.

7. Conclusions

We developed methods for mapping spatial variations of the SPS and SF slope for the first time, with the goal of connecting the H I statistical properties with the underlying turbulent drivers. The high spatial resolution provided by the ATCA and the ASKAP enabled us to reach the spatial scales where stellar feedback is predicted to significantly modify the turbulent H I spectrum.

1. With the rolling SPS and SF methods, we find that H I in the SMC has highly uniform turbulent properties. This could be due to stellar feedback effects that are mitigated by low metallicity, either by requiring even higher resolution observations as clouds become more compact, or because our statistical methods are not able to isolate the exact turbulent modes at play. Alternatively, a large line-of-sight depth of the SMC could be washing out localized (both in space and velocity) effects of stellar feedback.
2. The rolling SPS method revealed significant spatial variations of the SPS slope across the LMC. Throughout most of the LMC, the SPS requires a double power-law fit because of the H I disk structure. In agreement with previous studies, we find a more shallow slope on large

spatial scales. On spatial scales smaller than 200–300 pc, we have discovered several regions with localized steepening of the SPS slope. The most prominent such region is 30 Doradus. This steepening of the SPS slope is predicted by numerical simulations as a result of stellar feedback that erodes and destroys small clouds, effectively modifying the turbulent spectrum. Our results represent the first direct evidence for stellar feedback influencing the turbulent spectrum around large H II regions.

3. In the outskirts of the LMC, the rolling SPS method revealed two elongated localized regions of a very steep SPS slope. The southwest region is at the position where stellar disk of the LMC has a warp. As numerical simulations suggest that both stellar and H I disks should be warped and flaring, the steep SPS slope is likely tracing the transition from 2D to 3D turbulence due to the increase of the H I disk scale height. The southeast region coincides with the leading edge of the LMC, where theoretical and numerical studies have suggested significant ram-pressure effects as the LMC disk interacts with the MW halo.

S.S. acknowledges the support provided by the NSF Early Career Development (CAREER) Award AST-1056780, the Vilas funding provided by the University of Wisconsin, and the John Simon Guggenheim fellowship. This research was partially supported by the Munich Institute for Astro- and Particle Physics (MIAPP) of the DFG cluster of excellence "Origin and Structure of the Universe." N.Mc.-G. acknowledges funding from the Australian Research Council via grant FT150100024. We gratefully acknowledge contributions by W. Raja & K. Bannister to ASKAP commissioning. N.Mc.-G. also acknowledges support from the Diermeier visiting program at the University of Wisconsin. The authors thank the anonymous referee for constructive comments and suggestions. The authors are grateful to Daniel Eck, Diego Gonzalez Casanova, Eric Koch, Kearn Grisdale, Chad Bustard, Jay Gallagher, Bruce Elmegreen and Elena D'Onghia, for stimulating discussions. The Australian SKA Pathfinder is part of the Australia Telescope National Facility which is managed by CSIRO. Operation of ASKAP is funded by the Australian Government with support from the National Collaborative Research Infrastructure Strategy. ASKAP uses the resources of the Pawsey Supercomputing Centre. Establishment of ASKAP, the Murchison Radio-astronomy Observatory and the Pawsey Super-computing Centre are initiatives of the Australian Government, with support from the Government of Western Australia and the Science and Industry Endowment Fund. We acknowledge the Wajarri Yamatji people as the traditional owners of the Observatory site. The Australia Telescope Compact Array and the Parkes Radio Telescope are part of the Australia Telescope, which is funded by the Commonwealth of Australia for operation as a National Facility managed by CSIRO. The Magellanic Clouds Emission Line Survey (MCELS) data are provided by R. C. Smith, P. F. Winkler, and S. D. Points. The MCELS project has been supported in part by NSF grants AST-9540747 and AST-0307613, and through the generous support of the Dean B. McLaughlin Fund at the University of Michigan, a bequest from the family of Dr. Dean B. McLaughlin in memory of his lasting impact on Astronomy. This research made use of Astropy, a community-developed core Python package for Astronomy. Parts of this research were conducted by the Australian Research Council Centre of Excellence for All Sky Astrophysics in 3 Dimensions (ASTRO 3D), through project number CE170100013.

Software: Astropy (Astropy Collaboration et al. 2013), MIRIAD (Sault et al. 1995), KARMA (Gooch 1996), SciPy (Oliphant 2007), NumPy (van der Walt et al. 2011), Matplotlib (Hunter 2007).

Appendix
SPS Simulations

To effectively gauge the ability of the rolling SPS method to discern differing power indices, we used fBm-simulated images. We ran the rolling SPS routine on both single power-law simulated images with $\gamma = -2.7$ and -3.7, but also on a simulated image constructed of a broken power law with $\gamma = -3.7$ for small scales and -2.7 at the large-scale end, where the break point in the power law corresponded to a scale of 9 pixels. Simulated images were 655 by 655 pixels in size. This broken power-law image was constructed to simulate the H I SPS of the LMC as found by Elmegreen et al. (2001). In Figure 13 we present the effectiveness of our rolling SPS method with the F-test to reproduce the SPS index value, as well as the break-point location, when applied to simulated images.

The top row of Figure 13 shows results for a simulated image with a double power law, while the middle and bottom rows show results from single-slope simulated images, with $\gamma = -3.7$ and -2.7, respectively. The left column shows the results of the rolling SPS calculation: estimated small-scale slope in blue, large-scale slopes in green, and in red the single-slope values when the F-test indicated that a single-slope solution is preferred. Dash-dotted lines show the input slope values. The right column shows the estimated break-point values when the F-test preferred a two-slope solution.

There are two main conclusions from these tests. First, the F-test correctly decides that the simulated double power-law image (top row) has two slopes, while two single power-law simulated images are found to have predominantly single slopes. For single power-law simulated data (middle and bottom rows), we see that the preferred break point is typically limited to the shortest possible break point. However, we see a large increase in the number of preferred single-slope solutions (red). The dashed black line in the second and third row shows the sum of the three histograms (blue, green, and red) to illustrate that the overall preferred solution is near the input slope value.

Second, in all three cases, the recovered slopes are slightly underestimated (steeper than the original input slope). This is a consequence of the Gibbs effect on individual kernels, which affects more larger scales, resulting in a steeper slope. Figure 14 shows that as the kernel size increases and approaches the 655×655 pixel image size, the standard deviation in these results decreases and the slope distribution peak shifts closer to the input values. By doing these tests, we conclude that our estimated slopes for our kernel size of 1.5 kpc are systematically underestimated by $\sim$0.2.

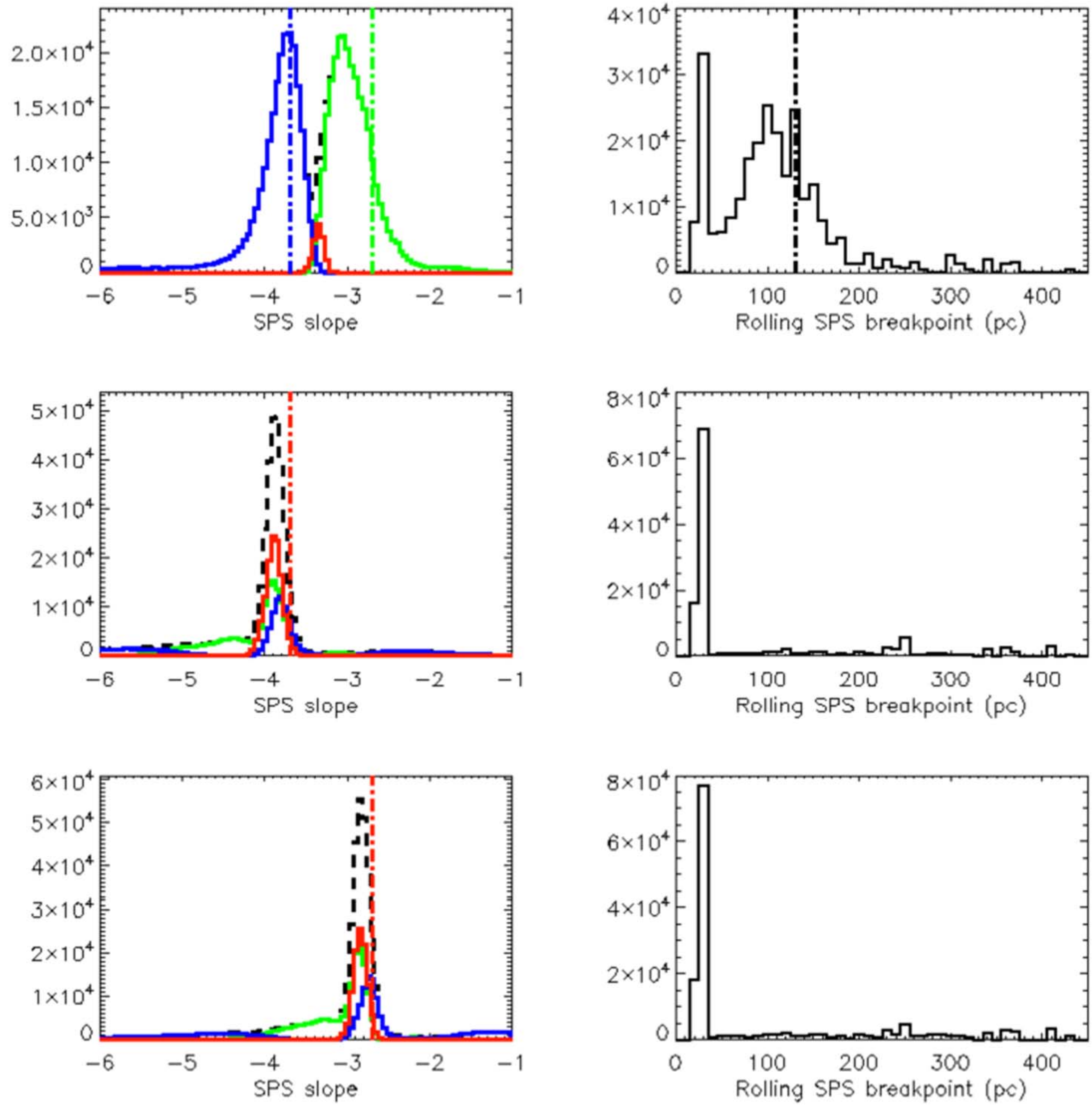

Figure 13. Results of the rolling SPS method when applied on fBm-simulated images. Each simulated image had a size of 655 × 655 pixels. A rolling SPS routine was performed with a kernel size of 128 pixels, shifted by 1 pixel. Single and double power-law fits were then calculated along with an F-test of the significance between the two fits. The F-test cutoff value was set at 0.05 significance. (Top) Simulated image with a double power law, with a slope of −3.7 on small scales and a slope of −2.7 on large scales, with the break point corresponding to 130 pc (or 9 pixels, we use a conversion of 1 pixel corresponding to 14.5 pc). The left column shows the results of the rolling SPS calculation: estimated small-scale slope in blue, large-scale slopes in green, and in red the single-slope values when the F-test indicated that a single-slope solution is preferred. Dash-dotted lines show the input slope values. The right column shows the estimated break-point values when the F-test preferred a two-slope solution. (Middle) Simulated image with a single power law of −3.7. (Bottom) Simulated image with a single power law of −2.7.

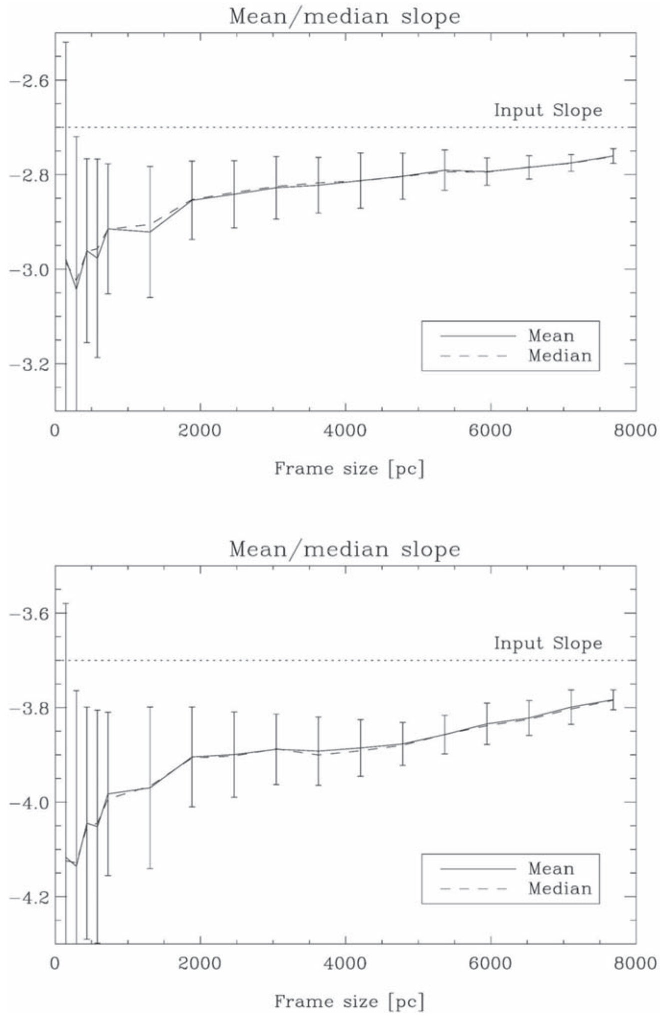

Figure 14. Example of how the kernel size affects calculations of the SPS slope. Two simulated fBm images are shown with an input SPS slope of −2.7 (top) and −3.7 (bottom). The *x*-axis shows the kernel size used to calculate the SPS slope. The kernel size varies from 500 pc to the full image size. By applying a given kernel size across the whole image, we estimate the median/mean SPS slope. As the kernel size increases, the recovered SPS slope from the rolling SPS method approaches the true input SPS slope.

ORCID iDs

Brian Babler https://orcid.org/0000-0002-6984-5752
N. M. McClure-Griffiths https://orcid.org/0000-0003-2730-957X
Alberto Bolatto https://orcid.org/0000-0002-5480-5686
Katherine Jameson https://orcid.org/0000-0001-7105-0994
Lister Staveley-Smith https://orcid.org/0000-0002-8057-0294

References

Alves, D. R., & Nelson, C. A. 2000, ApJ, 542, 789
Astropy Collaboration, Robitaille, T. P., Tollerud, E. J., et al. 2013, A&A, 558, A33
Besla, G., Kallivayalil, N., Hernquist, L., et al. 2012, MNRAS, 421, 2109
Block, D. L., Puerari, I., Elmegreen, B. G., & Bournaud, F. 2010, ApJL, 718, L1
Bolatto, A. D., Leroy, A. K., Jameson, K., et al. 2011, ApJ, 741, 12
Bournaud, F., Elmegreen, B. G., Teyssier, R., Block, D. L., & Puerari, I. 2010, MNRAS, 409, 1088
Bracewell, R. N. 2006, Fourier Analysis and Imaging (Berlin: Springer)
Braun, R. 2012, ApJ, 749, 87
Burkhart, B., Stanimirović, S., Lazarian, A., & Kowal, G. 2010, ApJ, 708, 1204
Calzetti, D., Kennicutt, R. C., Engelbracht, C. W., et al. 2007, ApJ, 666, 870
Choi, Y., Nidever, D. L., Olsen, K., et al. 2018, ApJ, 866, 90
Combes, F., Boquien, M., Kramer, C., et al. 2012, A&A, 539, A67
Cornwell, T. J., Humphreys, B., Lenc, E., Voronkov, M., & Whiting, M. T. 2011, ASKAP Science Processing: Askap-sw-0020 Tech. Rep. 028 (ASKAP Science Case Memo Series, CSIRO, 2011), CSIRO
Crovisier, J., & Dickey, J. M. 1983, A&A, 122, 282
de Avillez, M. A., & Breitschwerdt, D. 2005, A&A, 436, 585
Dickey, J. M., Mebold, U., Stanimirovic, S., & Staveley-Smith, L. 2000, ApJ, 536, 756
Dufour, R. J. 1984, in IAU Symp. 108, Structure and Evolution of the Magellanic Clouds, ed. S. van den Bergh & K. S. D. de Boer (Dordrecht: Kluwer), 353
Dutta, P., Begum, A., Bharadwaj, S., & Chengalur, J. N. 2009a, MNRAS, 397, L60
Dutta, P., Begum, A., Bharadwaj, S., & Chengalur, J. N. 2009b, MNRAS, 398, 887
Elmegreen, B. G. 2000, ApJ, 527, 266
Elmegreen, B. G., Elmegreen, D. M., & Leitner, S. N. 2003, ApJ, 590, 271
Elmegreen, B. G., Kim, S., & Staveley-Smith, L. 2001, ApJ, 548, 749
Elmegreen, B. G., & Scalo, J. 2004, ARA&A, 42, 211
Federrath, C., & Klessen, R. S. 2012, ApJ, 761, 156
Gaustad, J. E., McCullough, P. R., Rosing, W., & Van Buren, D. 2001, PASP, 113, 1326
Gooch, R. 1996, in ASP Conf. Ser. 101, Astronomical Data Analysis Software and Systems V, ed. G. H. Jacoby & J. Barnes (San Francisco, CA: ASP), 80
Gordon, K. D., Meixner, M., Meade, M. R., et al. 2011, AJ, 142, 102
Green, D. A. 1993, MNRAS, 262, 327
Grisdale, K., Agertz, O., Renaud, F., et al. 2019, MNRAS, 486, 5482
Grisdale, K., Agertz, O., Renaud, F., & Romeo, A. B. 2018, MNRAS, 479, 3167
Grisdale, K., Agertz, O., Romeo, A. B., Renaud, F., & Read, J. I. 2017, MNRAS, 466, 1093
HI4PI Collaboration, Ben Bekhti, N., Flöer, L., et al. 2016, A&A, 594, A116
Hou, T. Y., Wu, X.-H., Chen, S., & Zhou, Y. 1998, PhRvE, 58, 5841
Hunter, J. D. 2007, CSE, 9, 95
Jameson, K. E., Bolatto, A. D., Leroy, A. K., et al. 2016, ApJ, 825, 12
Jameson, K. E., McClure-Griffiths, N. M., Liu, B., et al. 2019, ApJS, 244, 7
Joung, M. K. R., & Mac Low, M.-M. 2006, ApJ, 653, 1266
Kim, J., Balsara, D., & Mac Low, M.-M. 2001, JKAS, 34, 333
Kim, S., Staveley-Smith, L., Dopita, M. A., et al. 1998, ApJ, 503, 674
Kim, S., Staveley-Smith, L., Dopita, M. A., et al. 2003, ApJS, 148, 473
Krumholz, M. R., & Burkhart, B. 2016, MNRAS, 458, 1671
Lazarian, A., & Pogosyan, D. 2000, ApJL, 537, 720L
Lazarian, A., & Pogosyan, D. 2004, ApJ, 616, 943
Levine, E. S., Blitz, L., & Heiles, C. 2006, ApJ, 643, 881
Mackey, D., Koposov, S., Da Costa, G., et al. 2018, ApJL, 858, L21
Maier, E., Chien, L.-H., & Hunter, D. A. 2016, AJ, 152, 134
Mastropietro, C., Burkert, A., & Moore, B. 2009, MNRAS, 399, 2004
McClure-Griffiths, N. M., Dénes, H., Dickey, J. M., et al. 2018, NatAs, 2, 901
Miville-Deschênes, M.-A., Levrier, F., & Falgarone, E. 2003, ApJ, 593, 831
Muller, E., Stanimirović, S., Rosolowsky, E., & Staveley-Smith, L. 2004, ApJ, 616, 845
Nayak, O., Meixner, M., Sewiło, M., et al. 2019, ApJ, 877, 135
Nestingen-Palm, D., Stanimirović, S., González-Casanova, D. F., et al. 2017, ApJ, 845, 53
Nikolaev, S., Drake, A. J., Keller, S. C., et al. 2004, ApJ, 601, 260
Offner, S. S. R., & Arce, H. G. 2015, ApJ, 811, 146
Oliphant, T. E. 2007, CSE, 9, 10
Olsen, K. A. G., & Salyk, C. 2002, AJ, 124, 2045
Orkisz, J. H., Pety, J., Gerin, M., et al. 2017, A&A, 599, A99
Padoan, P., Kim, S., Goodman, A., & Staveley-Smith, L. 2001, ApJL, 555, L33
Pingel, N. M., Lee, M.-Y., Burkhart, B., & Stanimirović, S. 2018, ApJ, 856, 136
Pingel, N. M., Stanimirović, S., Peek, J. E. G., et al. 2013, ApJ, 779, 36
Piontek, R. A., & Ostriker, E. C. 2005, ApJ, 629, 849
Putman, M. E., Staveley-Smith, L., Freeman, K. C., Gibson, B. K., & Barnes, D. G. 2003, ApJ, 586, 170
Ramachandran, V., Hamann, W.-R., Oskinova, L. M., et al. 2019, A&A, 625, A104
Russell, S. C., & Dopita, M. A. 1992, ApJ, 384, 508
Salem, M., Besla, G., Bryan, G., et al. 2015, ApJ, 815, 77

Sault, R. J., Teuben, P. J., & Wright, M. C. H. 1995, in ASP Conf. Ser. 77, Astronomical Data Analysis Software and Systems IV, ed. R. A. Shaw, H. E. Payne, & J. J. E Hayes (San Francisco, CA: ASP), 433
Simonetti, J. H., Cordes, J. M., & Spangler, S. R. 1984, ApJ, 284, 126
Smith, R. C., & Team, M. C. E. L. S. 1999, in IAU Symp. 190, New Views of the Magellanic Clouds, ed. Y.-H. Chu (San Francisco, CA: ASP), 28
Snedecor, G. W., & Cochran, W. G. 1989, Statistical Methods (Iowa City, IO: Univ. Iowa Press), 343
Stanimirović, S., & Lazarian, A. 2001, ApJL, 551, L53
Stanimirović, S., Staveley-Smith, L., Dickey, J. M., Sault, R. J., & Snowden, S. L. 1999, MNRAS, 302, 417
Stanimirović, S., Staveley-Smith, L., & Jones, P. A. 2004, ApJ, 604, 176
Stanimirović, S., Staveley-Smith, L., van der Hulst, J. M., et al. 2000, MNRAS, 315, 791
Staveley-Smith, L., Kim, S., Calabretta, M. R., Haynes, R. F., & Kesteven, M. J. 2003, MNRAS, 339, 87
Stilp, A. M., Dalcanton, J. J., Skillman, E., et al. 2013, ApJ, 773, 88
Tamburro, D., Rix, H.-W., Leroy, A. K., et al. 2009, AJ, 137, 4424
van der Marel, R. P., & Cioni, M.-R. L. 2001, AJ, 122, 1807
van der Walt, S., Colbert, S. C., & Varoquaux, G. 2011, CSE, 13, 22
Wada, K., Meurer, G., & Norman, C. A. 2002, ApJ, 577, 197
Walker, A. P., Gibson, B. K., Pilkington, K., et al. 2014, MNRAS, 441, 525
Warren, S. R., Skillman, E. D., Stilp, A. M., et al. 2012, ApJ, 757, 84
Westerlund, B. E. 1991, in IAU Symp. 148, The Magellanic Clouds, ed. R. Haynes & D. Milne (Dordrecht: Kluwer), 15
Yoo, H., & Cho, J. 2014, ApJ, 780, 99
Young, L. M., & Lo, K. Y. 1996, ApJ, 462, 203
Zhang, H.-X., Hunter, D. A., & Elmegreen, B. G. 2012, ApJ, 754, 29